MICROSTRUCTURE and CREEP RUPTURE of P92-grade weld metal

S.T. Mandziej, A. Výrostková and C. Chovet

ABSTRACT

The search for new more creep–resistant materials for supercritical components of modern power plants stimulates also welding research to provide joints adequate to withstand highly demanding operation conditions. Seeking for improvement of existing welding consumables, experimental Ti-doped P92 grade weld metals were developed of exceptionally long life in creep rupture tests. In response to this request SEM and TEM investigations were carried out to identify the features of microstructure, which could be responsible for so different behaviour in the creep rupture tests. In this research the microstructures of the Ti-doped FCAW P92 weld metals were also compared with these of a standard P92 pipe material as well as with the submerged arc weld metal deposit W0 manufactured by flux-cored consumable containing no addition of Ti. Transformation of microstructures of this "reference" P92 pipe material and of the Ti-free P92 weld metal was accomplished in the accelerated creep tests on Gleeble physical simulator. An attempt has been made to correlate the fracture appearance of the creep-ruptured samples with the fine structure in their head/grip and gauge portions. In the microstructure of non-affected by the creep strain head portions of the creep-ruptured samples appeared numerous delta-ferrite grains with no carbide precipitates. Evidences were found that creep voids and cracks formed fast in the initially precipitate-free delta-ferrite grains of the sample W1, while in sample W2 during the creep test a peculiar strain-induced precipitation hardening of the delta-ferrite appeared, however no Ti was identified there in the ultra-fine precipitates.

IIW-Thesaurus keywords: Carbides; Creep tests; Electron microscopy; Microstructure.

1 Introduction

The challenge for stronger and better creep resistant steels and welds continues and, in this field, numerous P92-grade weld metals containing various micro-additives were recently developed. Such development of welding consumables and manufacturing of welds from them faces one critical limit – the long time of creep testing required to verifying the performance of the welds. Accelerated creep tests or creep-rupture tests allow to speed-up the testing and offer results useful as feedback in the development procedure, provided that transformed microstructure does not differ from the truly crept one. One of such procedures, a low-cycle thermal-mechanical fatigue test developed on Gleeble physical simulator, allows in less than 50 h transforming the microstructure of steel or weld to a near-to-equilibrium one similar to that after a multi-year exposure [1]. Short-term constant load creep testing procedures can also accelerate the testing, and for this purpose often use increase of test temperature or testing under high stress, or both.

New generation martensitic creep-resisting steels of P91, P911, P92, and higher-Cr steel grades which are under development, exhibit adequate strength at elevated temperatures, however their nominal strength may be compromised by susceptibility to type-IV cracking in heat-affected zones of welds [2] while increasing contents of ferrite-forming elements may lead to excessive formation of delta-ferrite and associated decrease of creep strength and life [3].

The demand of higher welding productivity leads to semi-automatic arc welding procedures with flux-cored consumables, and in these strong ferrite-formers like Ti and Al additives are natural ingredients [4]. In search for an optimum chemical composition Cr-equivalent may be used, which for the value of less than 8 should guarantee no delta-ferrite [5]. The welding procedures next to the chemical compositions may significantly affect the initial microstructures of the weld metals and then influence the evolution of these microstructures during exposure to creep.

Recent research on Ti-doped P92 grade weld metals showed possible improvement of the P92 welds quality by optimum addition of Ti [6]. Depending on the Ti content these weld metals gave much different results of time to fracture. The developers of these weld metals, who presented their results at the COST-536 EU R and D action, invited the partners in the COST to carry out detailed electron-microscopic investigation in order to confirm possible strengthening of ferrite grains by uniformly distributed fine particles containing Ti [7].

2 Materials and procedures

In the research related to the COST-536 EU R and D action new P92 grade weld metals containing different amounts of Ti were manufactured, which in creep-rupture tests carried out at relatively high stress level of 216 MPa at 600 °C showed very different time to fracture. In particular the sample containing ~300 ppm of Ti failed after

Doc. IIW-2027, recommended for publication by Commission II "Arc Welding and Filler Metals."

~100 h, while the sample doped with ~600 ppm of Ti lasted for ~9 000 h [6]. To explain the reasons of such differences, it was requested to carry out detailed electron-microscopic investigation on selected samples of different Ti content with particular attention given to fine precipitates containing Ti. For comparison of microstructures, electron-microscopic observations were also carried out on a standard P92 pipe material (PM), as well as on Ti-free weld metal (W0), which due to its chemical composition should not contain the delta-ferrite. These "reference" pipe material and weld metal were taken from a contacted research of one of the partners [8]. The chemical compositions of the selected samples are given in Table 1.

Considering that the standard nitrogen content in P92 weld metal should be from 400 to 450 ppm, the Cr equivalent for all samples including W1 was calculated according to the following formula [9]:

Creq = % Cr + 6 % Si + 4 % Mo + 1.5 % W + 11 % V + 5 % Nb + 12 % Al + 8 % Ti – 40 % C – 2 % Mn – 4 % Ni – 2 % Co – 30 % N - % Cu

The standard P92 pipe steel (PM sample) and the "Ti-free" weld metal (W0 sample) were accelerated creep tested in Gleeble physical simulator; the selected P92 weld metal sample W0 had at the ACT temperature of 600 °C an average tensile yield stress of 208 MPa.

On the creep-ruptured samples, hardness was measured on head and gauge portions; the non-affected by creep strain head portion of sample W1 was for only 100 h exposed to temperature of 600 °C, while the head portion of sample W2 was exposed at this temperature for 9 000 h.

As regards the accelerated crept samples PM and W0, their head portions were during the tests kept in cold copper jaws, i.e. their temperature never exceeded 50 °C.

Vickers hardness tests were carried out on the mentioned portions of samples; 10 random indentations were made with 1 kgf load. The results of the hardness measurements are given in Table 2.

The fracture portions of the creep-ruptured samples were cut-off for fractographic observations in SEM; surface oxides were carefully removed from the fractures by electrochemical etching. Then, from the remaining parts of the creep-ruptured samples, specimens were prepared for classic optical metallography and microhardness measurements on microstructural components, after which carbon extraction replicas were taken from gauge and head portions of the creep-ruptured samples for microanalysis. The particles extracted in carbon replicas were examined in a Philips CM 12 TEM/STEM operating at 120 kV and equipped with an EDAX energy-dispersive x-ray microanalyser (EDX) with a Phoenix ultra-thin window detector, which allows to qualitatively analysing elements down to carbon and nitrogen. The particles were microanalysed for their chemical compositions, calculated form X-ray spectra by EDAX software for thin samples. No extra corrections for absorption of fluorescence were made. Particle identification was based on the semi-quantitative results by EDX combined with selected area diffraction.

In the next instance from the head portions and gauge portions of the creep-ruptured samples and from the ACT samples thin slices were cut-off for SEM microstructural investigations. After slicing by a low-speed precision diamond saw, the slices were electro-polished, then etched by ferric-chloride solution and subjected to SEM observations. On these slices microstructural features were sought, which were characteristic for creep voids and cracks appearance on fracture surfaces and just below them. From this way identified critical sites of the microstructure 3 mm diameter

Table 1

Sample	Element [wt. %]							
	C	Si	Mn	Cr	Mo	Ni	Co	Al
PM	0.08	0.23	0.95	9.1	0.44	0.22	0.00	0.008
W0	0.10	0.21	1.20	8.5	0.42	0.30	1.03	0.005
W1	0.11	0.29	0.56	9.5	0.43	0.37	0.02	0.011
W2	0.13	0.36	0.73	9.8	0.54	0.50	0.01	< 0.01

Sample	Element [wt. %]						
	Ti	Nb	W	V	N	B	Creq
PM	0.002	0.038	1.22	0.27	0.0386	26 ppm	10.2
W0	0.005	0.045	1.38	0.21	0.0421	10 ppm	5.8
W1	0.031	0.040	1.14	0.22	ND	23 ppm	10.6
W2	0.072	0.040	1.50	0.27	0.044	30 ppm	10.1

ND = not determined.

Table 2

Material	Sample	Average HV 1.0 at location	
		Head	Gauge
Weld metal P92 + 300 ppm Ti	W1	264	256
Weld metal P92 + 600 ppm Ti	W2	281	266
Rolled pipe P92	PM	268	228
Weld metal P92 with 2 % Co	W0	294	239

disks were punched out for the final preparation of thin foils to transmission electron microscopy. The preparation of thin foils for TEM observations was made in a twin-jet electro-polisher Struers Tenupol-5. The thin foils were examined in an analytical transmission microscope JEOL 200CX at an accelerating voltage of 200 kV. For identification of phases selected area electron diffraction as well as micro-beam diffraction were used. Specimens from all samples were examined this way for their precipitation characteristic and dislocation substructure. Considering that in the dislocation configurations large amount of their components/segments might be highly mobile, very high illumination conditions were used in TEM to observe and record true dislocation substructures at the foils thicknesses from 320 to 470 nm.

3 Results

3.1 Fractography of P92 creep-ruptured W1 and W2 samples

After electrochemical removal of oxides from the fracture surfaces of the creep-ruptured samples W1 and W2, the creep voids and microstructure features were revealed. In sample W1 carbide-free regions could be observed (Figure 1) at which large creep voids appeared and through which secondary narrow cracks formed. The carbide distribution in sample W2 on the fracture surface is quite uniform and this is characteristic for all components of microstructure (Figure 2); arrays of the creep voids seem to follow the prior austenite grain boundaries. Coagulation of carbides at the fracture surface of sample W1 (Figure 3) is less advanced than in sample W2 (Figure 4), certainly due to the much longer exposure time of W2 at the creep-rupture test temperature. The medium-size creep voids formed in sample W2 seem to be associated with clusters of carbides along prior austenite grain boundaries (Figure 4) while some larger equi-axed voids in sample W1 can be attributed to the spheroidal slag inclusions (Figure 3). The largest elongated secondary cracks in sample W1 always run through the precipitate-free ferritic grains of type-IV or delta-ferrite origin (Figures 3 and 5). On etched fracture surface of sample W2 small, recrystallized ferrite grains are visible (Figure 6).

3.2 Microstructures of P92 weld metals W1 and W2

By light microscopy three major components of the high-tempered microstructure were observed: long columnar crystals filled with post-martensitic laths, granular crystals

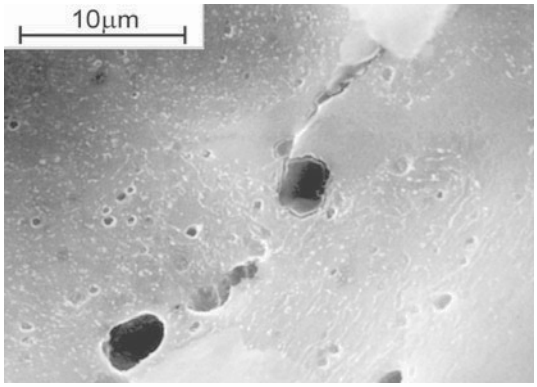

Figure 1 – Electro-etched fracture surface of sample W1; fine creep voids in former martensite and large creep voids and shear-type crack through precipitate-free ferrite grains; SEM image

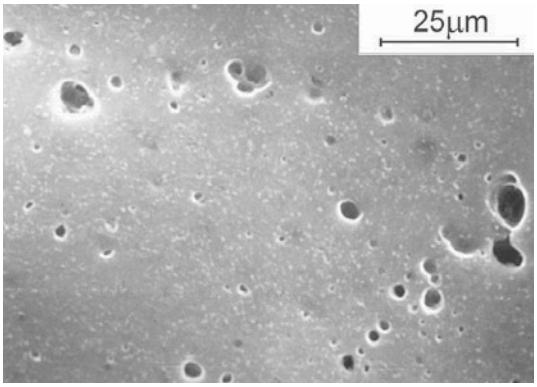

Figure 2 – Electro-etched fracture surface of sample W2; uniformly distributed carbides and arrays of creep voids preferentially along former austenite grain boundaries; SEM image

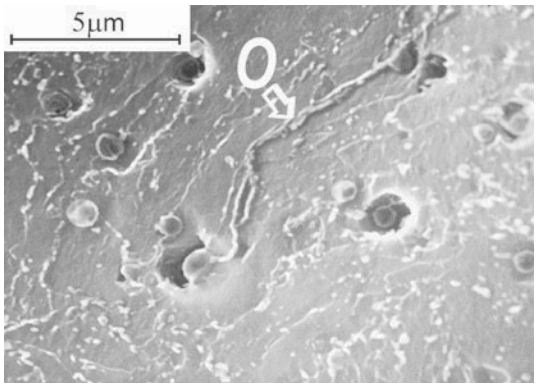

(O – non-removed oxide in the shear-crack.

Figure 3 – $FeCl_3$ etched fracture surface of sample W1; creep voids at inclusions and shear-crack in precipitate-free ferrite; SEM image

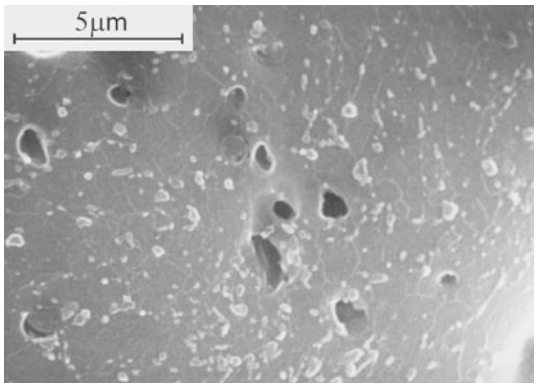

Figure 4 – Electro-etched fracture surface of sample W2; uniformly distributed large carbide precipitates and creep voids formed at clusters of the carbide precipitates; SEM image

with well-pronounced boundaries of former austenite, and δ-ferrite grains. At larger magnifications, as examined in SEM on cross-sections taken from head portions of the creep-ruptured samples, in the high-tempered post-martensitic microstructures some characteristic differences between weld metals W1 and W2 could be distinguished. The microstructure of sample W1 is more coarse-grained (Figure 7) as compared with W2 (Figure 8), having larger widths of post-martensitic laths and the carbide precipitation less advanced than in sample W2. The last is obviously due to much longer exposure of sample W2 at 600 °C, i.e. 9 000 h instead of 100 h. Characteristic of sample W1 are narrow elongated "clean" ferrite areas entirely free of precipitates, not existing in this form in sample W2. Their locations were mostly in inter-bead HAZs along interfaces between columnar and granular crystals, which suggest they are "type-IV" ferrite. In sample W2 similar features have boundaries covered by chains of precipitates (Figure 9). Granular δ-ferrite grains appear in both samples, somewhat larger in sample W1 (Figure 10).

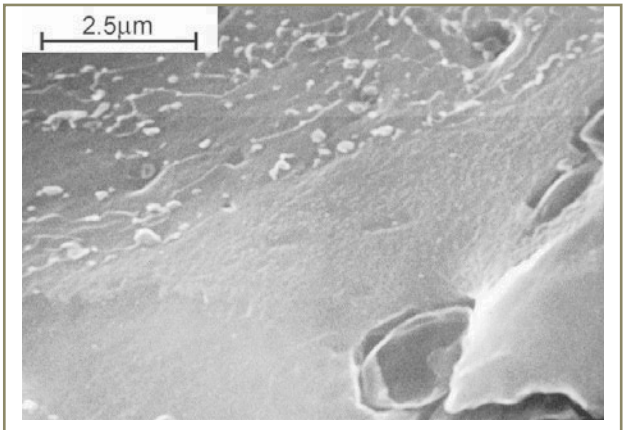

Figure 5 – $FeCl_3$ etched fracture surface of sample W1; large precipitate-free δ-ferrite grain with void and elongated creep crack; SEM image

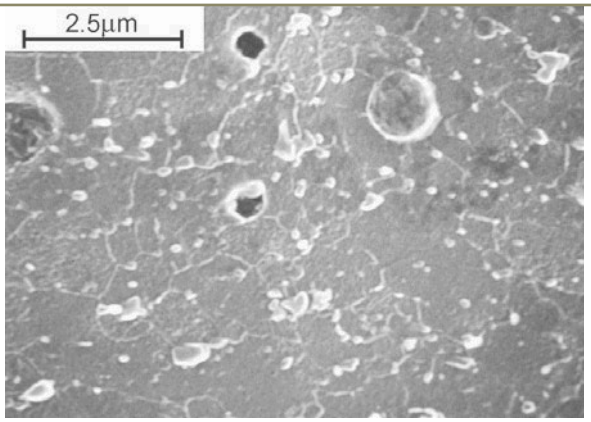

Figure 6 – $FeCl_3$ etched fracture surface of sample W2; clusters of coagulated carbides and fine recrystallized ferrite grains; SEM image

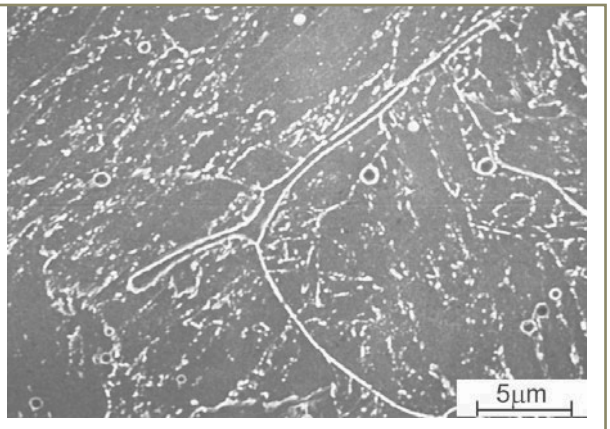

Figure 7 – Tempered martensite of sample W1 with narrow precipitate-free ferritic feature along prior austenite grain boundary; SEM image

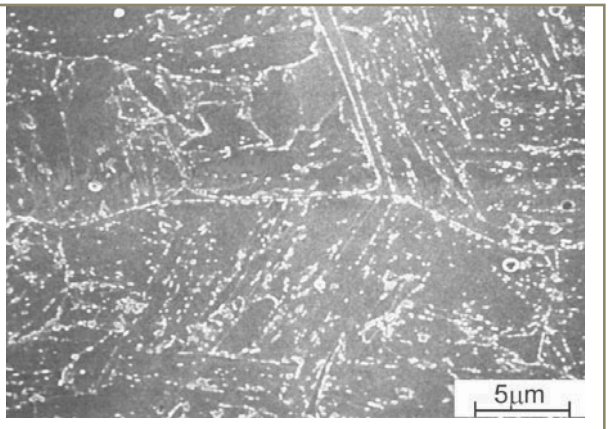

Figure 8 – Tempered martensite of sample W2; prior austenite grain boundaries traced by chains of precipitates; SEM image

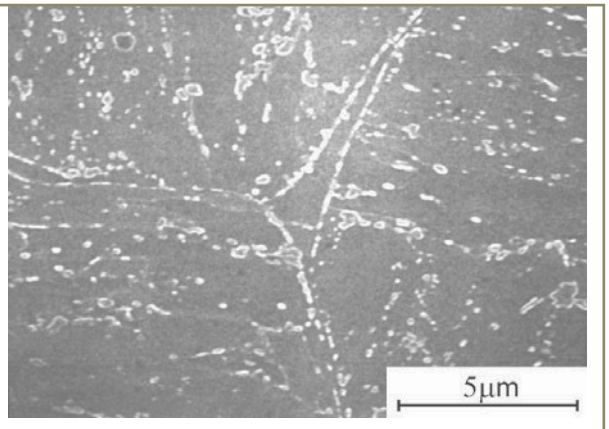

Figure 9 – Sample W2; wedge shaped ferrite grain with boundaries covered by carbides; SEM image

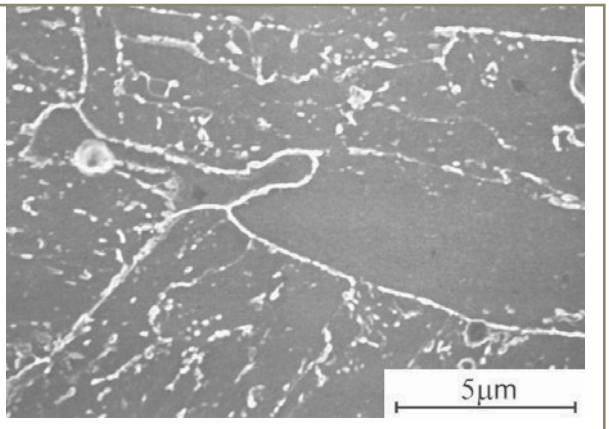

Figure 10 – Sample W1; precipitate-free δ-ferrite grain surrounded by tempered martensite; SEM image

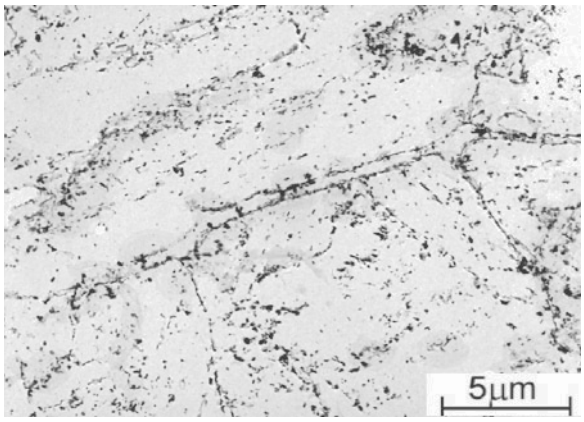

Figure 11 – Distribution of carbides along prior austenite grain boundaries in sample W1; carbon extraction replica – TEM

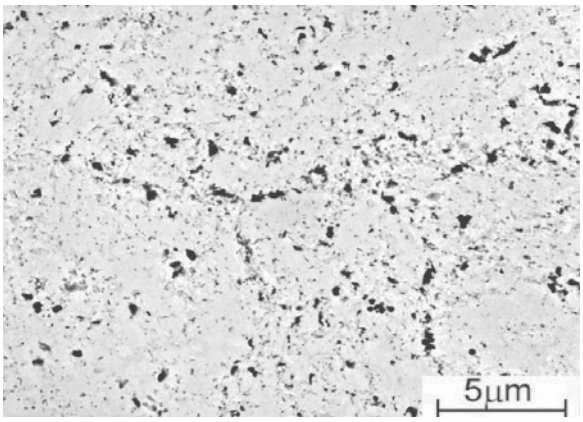

Figure 12 – High density of fine carbides and larger carbides tracing boundaries of re-austenitized grains in sample W2; carbon replica – TEM

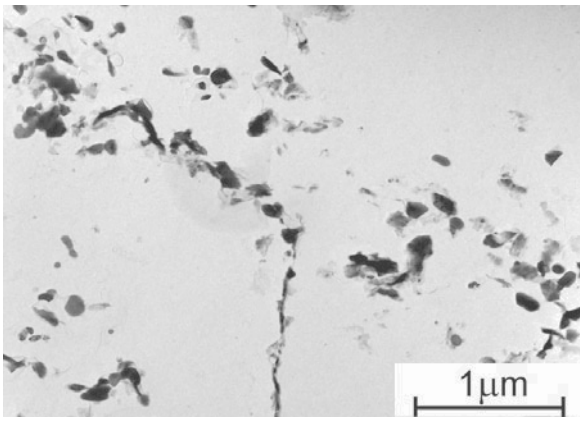

Figure 13 – Carbides around precipitate-free ferrite in sample W1; carbon replica – TEM

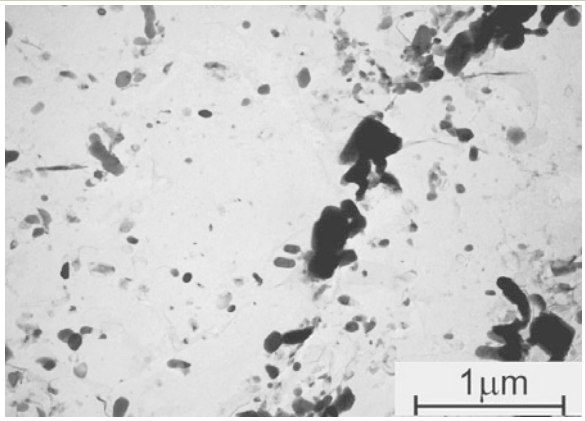

Figure 14 – Distribution of various size carbides in sample W2; carbon replica – TEM

In the gauge portion of the creep-ruptured weld W1 dominates a non-homogeneous precipitation and "type-IV" features appear well preserved (Figure 11), while in weld W2 the precipitation is more uniform and at locations of re-austenitized globular grains much more intensive (Figure 12). At larger magnifications can be seen that in sample W1, next to agglomerates of carbides, precipitate-free ferrite areas are present (Figure 13) while in sample W2 precipitates of various sizes are present almost everywhere (Figure 14).

The observations on carbon replicas showed the intensive precipitation along former austenite grain boundaries, as well as along the former martensite laths. In the gauge portions of samples W1 and W2 the particles seem to be a little larger than in the head portions and the shapes of the laths begin to disappear. The particles on the replicas were identified by electron diffraction supplemented by EDX microanalysis. The chemical composition of analysed phases is given in Table 3.

The largest amount of the particles observed in the microstructure were the $M_{23}C_6$ carbides, appearing as a complex Cr-Fe-W-Mo compounds mostly in the shape of ovals having the sizes from 30 nm up to 300 nm, often forming agglomerates along prior austenite grain boundaries. Next to this major secondary phase in somewhat lesser amount appeared MX particles identified as V-Nb rich carbonitrides. In sample W1 their size ranges from 80 nm ovals up to 250 x 150 nm foil shaped particles. They are embedded at the lath boundaries mainly, often having the shapes of thin rods. The MX particles in sample W2 have visibly lower size (50-100 nm) and the shape of rods. The largest identified particles, appearing

Table 3

Sample	$M_{23}C_6$ weight percent	MX weight percent	Laves Ph. weight percent
W1 - gauge	58Cr-24Fe-9W-6Mo-3V+Nb	62V-14Nb-18Cr-4Fe-2Mo	26Fe-15Cr-41W-14Mo-3Nb+V
W1 - head	56Cr-23Fe-13W-6Mo-2V+Nb	58V-22Nb-14Cr-2Fe-3Mo	33Fe-7Cr -39W-19Mo-2Nb+V 48Fe-14Cr-9W-27Mo-3V+Nb 44W-18Mo-26Fe-8Cr-3Nb+V
W2 - gauge	60Cr-21Fe-9W-6Mo-4V+Nb	61V-21Nb-14Cr-1Fe-3Mo	29Fe-7Cr-47W-15Mo-2Nb+V
W2 - head	61Cr-20Fe-11W-5Mo-4V+Nb	60V-20Nb-12Cr-5Fe-3Mo 52V-38Nb-8Cr-1Fe-1Mo	27Fe-7Cr-48W-15Mo-2Nb+V

Table 4

Sample	Microhardness of components μHV 0.1					
	Head portion grains			Gauge portion grains		
	δ-ferrite	columnar	globular	δ-ferrite	columnar	globular
W1	238	269	261	244	258	239
W2	**258**	282	282	**273**	267	264

rather seldom in the microstructure, were Laves phases having sizes up to 300 nm in sample W1 and up to 600 nm in sample W2. In the investigated weld metals their compositions varied from W-rich to Mo-rich, i.e. from $(Fe, Cr)_2(W, Mo)$ type to $(Fe, Cr)_2(Mo, W)$ type, with a small amounts of Si and traces of other elements like Nb and V. The Laves phases precipitated predominantly at former austenite grain boundaries, often in close vicinity of Cr-rich particles, i.e. $M_{23}C_6$ carbides. No Ti-rich secondary precipitates have been found; substantial amounts of Ti have been only analysed in spheroidal slag inclusions. The compositions of phases in both W1 and W2 samples did not show any difference between gauge and head portions. To supplement the microstructural observations, microhardness was tested with the load of 100 g, i.e. the largest allowing measurements on individual microstructure components: columnar crystals, globular crystals and δ-ferrite. The results are given in Table 4.

3.3 Fine structure of P92 weld metal W1

In the head portion of the creep-ruptured sample W1, i.e. the portion which was only annealed for ~100 h without being subjected to creep stress, tempered martensite microstructure dominated (Figure 15) with very high dislocation density in partly recovered subgrains (Figure 16). In such matrix spheroidal oxide inclusions are present as well as numerous carbides deposited mainly along the former martensite lath boundaries and austenite grain boundaries.

Thin elongated ferritic features are locally present, in particular near to inter-bead heat-affected zones (type-IV zones), having larger coagulated carbides deposited at their borders (Figure 17) as well as some finer ones within the borders. This type of ferrite contains very few dislocations neither any precipitates inside. In the largest δ-ferrite grains high-density configurations of criss-crossing *a* / 2<111> screw dislocations with numerous jogs were observed (Figure 18);

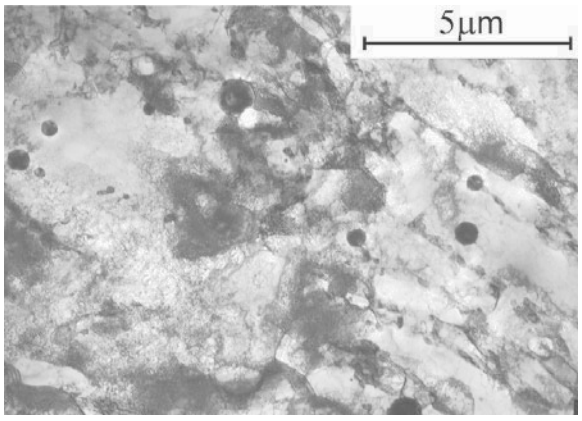

Figure 15 – Tempered martensite/bainite with very high dislocation density and precipitates at subgrain borders; sample W1, TEM, thin foil

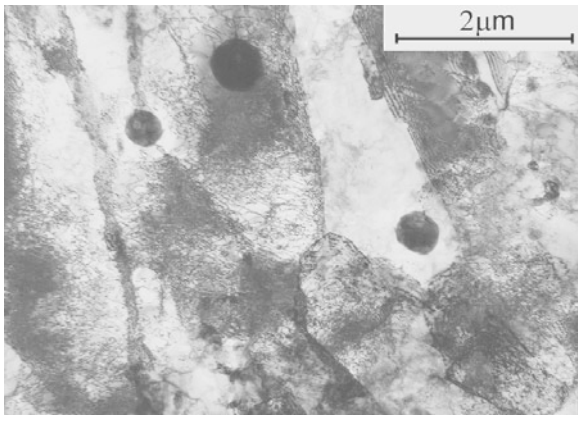

Figure 16 – Subgrains with very high dislocation density and spheroidal slag inclusions; sample W1, TEM, thin foil

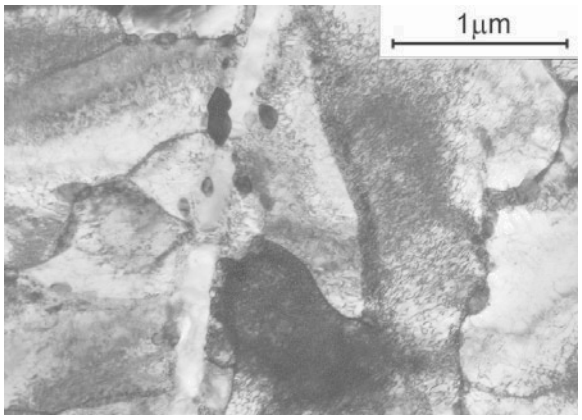

Figure 17 – Narrow ferritic "type-IV" feature of low dislocation density next to small semi-recovered ferrite grains with high dislocation density; sample W1, TEM, thin foil

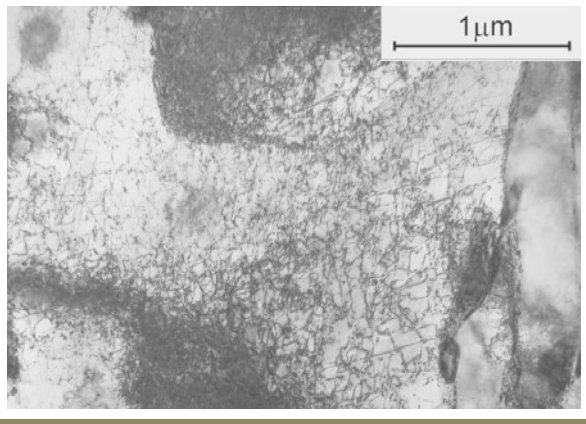

Figure 18 – δ-ferrite grain with high density of criss-crossing dislocations locally pinned by ultra-fine precipitates; sample W1, TEM, thin foil

at some locations ultra-fine precipitates were found pinning such dislocations.

In the gauge portion of the creep-ruptured sample W1, the matrix consists of fully recovered equi-axial and elongated subgrains as well as of fine recrystallized grains of ferrite (Figure 19). Recrystallization occurs by coalescence of subgrains and is most advanced near to the large spheroidal (slag) inclusions (Figure 20). The coalescence of many subgrains seems retarded by chains of carbides deposited at their borders (Figure 21), while numerous of these borders consist of dislocation arrays. No more high dislocation density can be seen inside the ferrite subgrains or recrystallized grains. The characteristic elongated type-IV ferrite features have their borders pinned by very high-density colonies of fine platelike carbides and contain almost dislocations inside (Figure 22). The $M_{23}C_6$ type carbides dominate in these microstructures and in somewhat lesser amount appear MX carbonitrides. Only few thin plate-like M_6C were found within the carbide agglomerates at the grain and subgrain boundaries. Also the Laves phase precipitates were rare, although quite large as compared with the carbides.

3.4 Fine structure of P92 weld metal W2

In the head portion of the creep-ruptured sample W2 a tempered martensite appears with well pronounced and traced by numerous carbides former austenite grain boundaries (Figure 23), larger ferrite grains with very high dislocation density are present too (Figure 24).

The post-martensitic matrix consists of semi-recovered ferrite subgrains with very high-density configurations of tangled dislocations, next to which ferrite regions exist. Larger coagulated carbides appear in forms of arrays or colonies, the last mainly at triple-points between the former austenite grains. Subgrain and grain boundaries are in many instances pinned by chains or arrays of medium-sized carbides (Figure 25). The carbides along grain boundaries are mainly identified as of $M_{23}C_6$ type, the MX phase appear there as well. In agglomerates of larger carbides having coagulated semi-spheroidal form, next to the $M_{23}C_6$ carbides few large particles of Laves phase were found (Figure 26). The large $M_{23}C_6$ carbides often possess internal substructure, suggesting that certain dislocations could be cutting through them.

Microstructure in the gauge portion of the creep-ruptured sample W2 consists of quite well recrystallized ferrite matrix with various sizes of grains and subgrains, and with numerous medium-sized carbides of semi-spheroidal form (Figures 27 and 28). Most of the dislocation-type subgrain walls, which dominate in the substructure, contain fine carbide precipitates and are pinned by them.

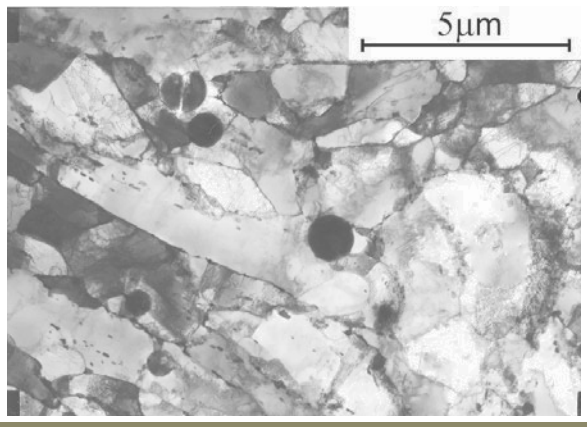

Figure 19 – Recovered/recrystallized subgrains and grains of ferrite in gauge portion of sample W1; TEM, thin foil

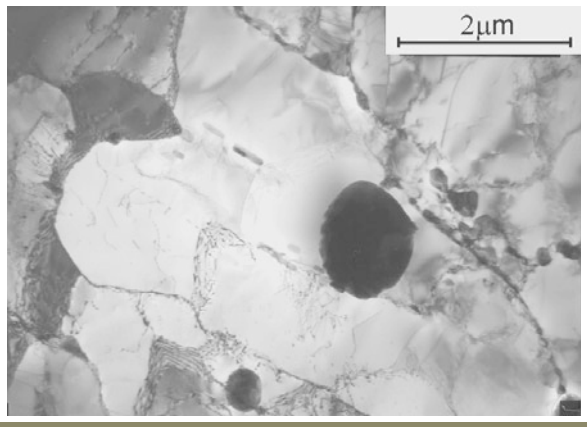

Figure 20 – Small recrystallized ferrite grain around spheroidal slag inclusion; sample W1, TEM, thin foil

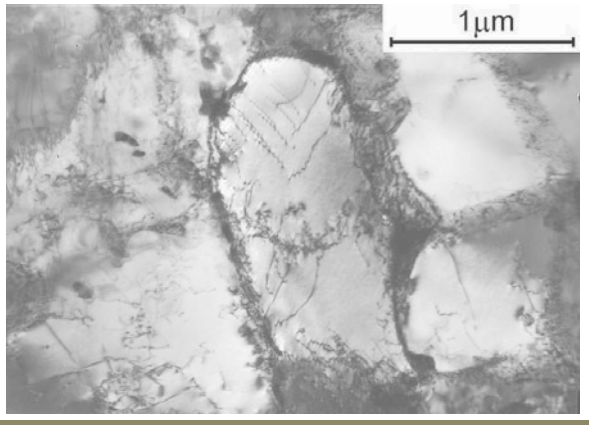

Figure 21 – Fine carbides at and inside borders of recovered subgrain; sample W1, TEM, thin foil

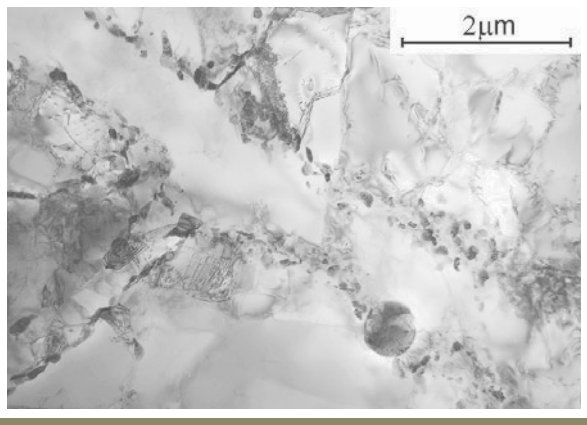

Figure 22 – Fine carbides inside borders of elongated ferritic feature; sample W1, TEM, thin foil

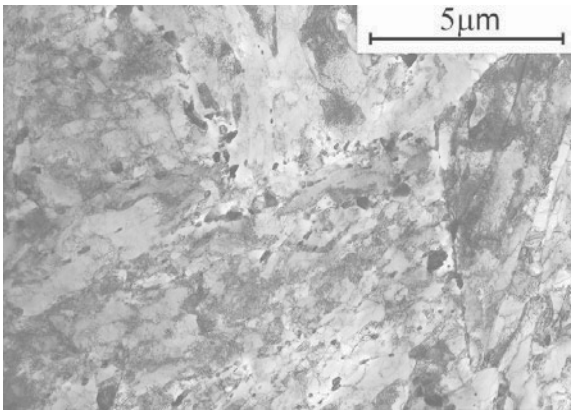

Figure 23 – Tempered martensite consisting of subgrains with very high dislocation density; sample W2, TEM, thin foil

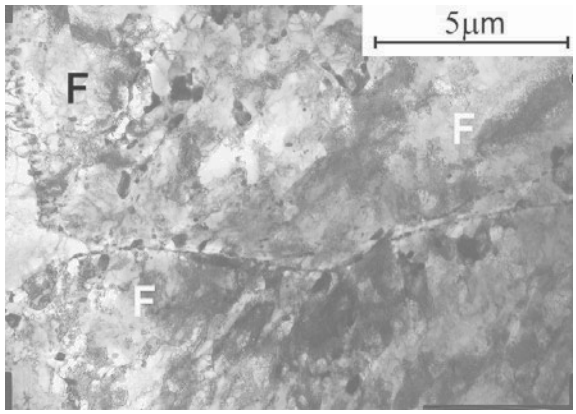

Figure 24 – Tempered martensite and ferrite (F) with very high dislocation density; sample W2, TEM, thin foil

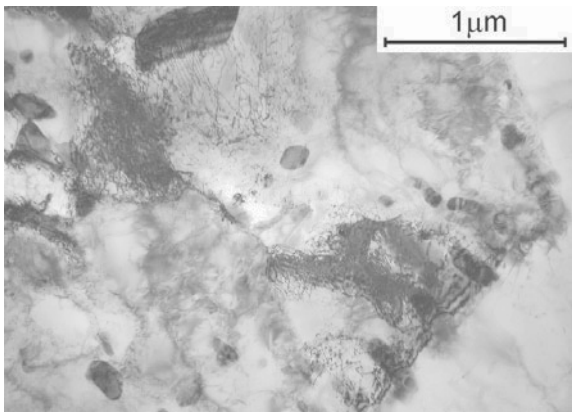

Figure 25 – High-angle boundary of ferritic grain pinned by array of carbides; sample W2, TEM, thin foil

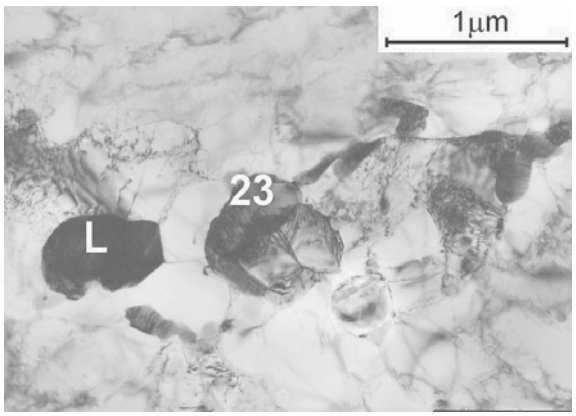

Figure 26 – Large coagulated particles of $M_{23}C_6$ carbide (23) and Laves phase (L) in recovered ferrite matrix; sample W2, TEM, thin foil

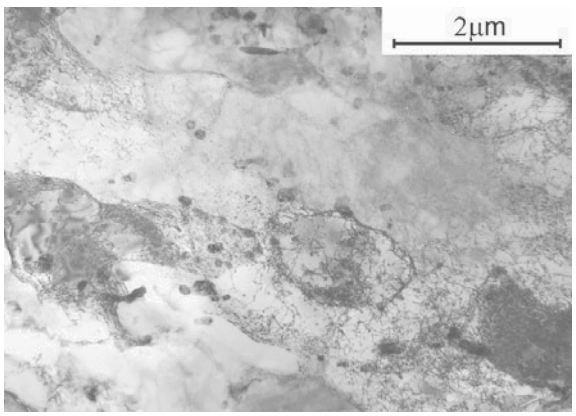

Figure 27 – Recovered/recrystallized ferrite matrix with semi-spheroidized carbides; sample W2, TEM, thin foil

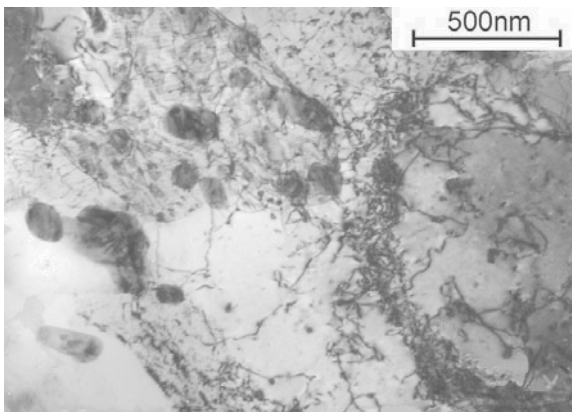

Figure 28 – Semi-spheroidized carbides within dislocation-type boundaries of ferrite subgrains; sample W2, TEM, thin foil

In larger recrystallized ferrite grains as well as in the δ-ferrite grains appear characteristic arrays of criss-crossing dislocations pinned by ultra-fine particles, in particular close to high-angle ferrite grain boundaries (Figures 29 and 30).

Closer to the neck portion of the sample W2 the ferrite subgrains and grains contain high density configurations of partly recovered dislocations and large amount of the very fine precipitates pinning these dislocations. Possibly due to higher localized strain, the generation of deformation dislocations and then their recovery assisting strain-induced precipitation are here observed (Figures 31 and 32).

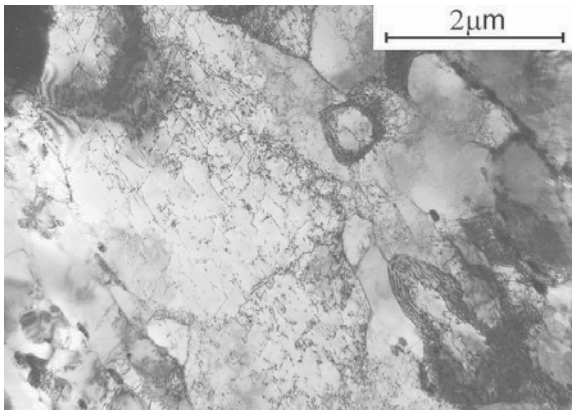

Figure 29 – Criss-crossing dislocations in recrystallized ferrite grain near to prior austenite grain boundary; sample W2, TEM, thin foil

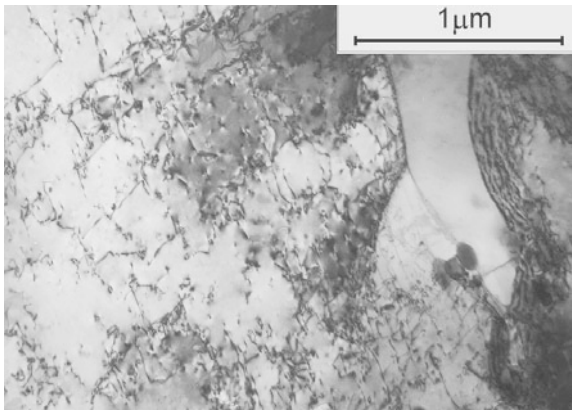

Figure 30 – Configuration of criss-crossing dislocations interacting with ultra-fine precipitates; sample W2, TEM, thin foil

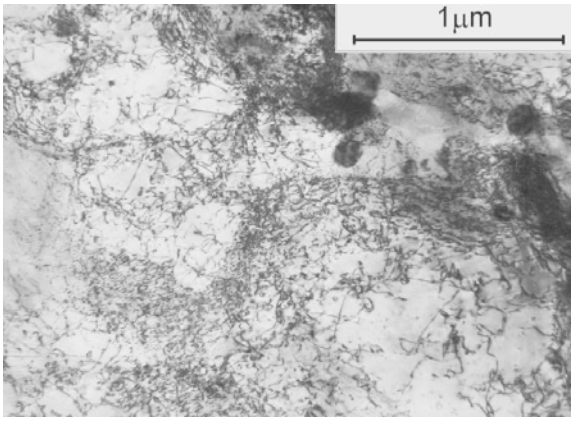

Figure 31 – Ferrite subgrains with high dislocation density in the neck portion of sample W2; TEM, thin foil

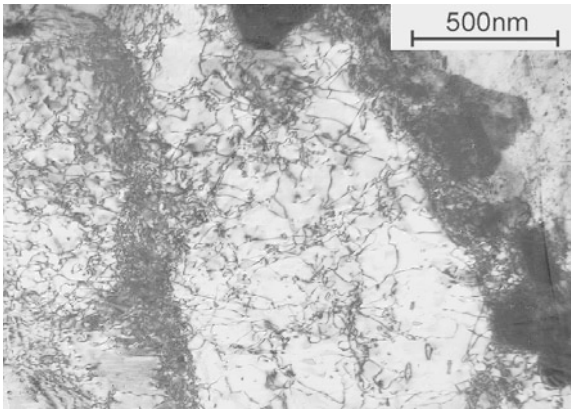

Figure 32 – Dislocations pinned by ultra-fine precipitates inside a subgrain; neck portion of sample W2, TEM, thin foil

3.5 Microstructures of P92 reference materials

3.5.1 Microstructure of P92 pipe steel, sample PM

In the initial state, i.e. before the ACT, the microstructure of P92 pipe steel is of high-tempered martensite with precipitated carbides tracing prior austenite grain boundaries and boundaries of former martensite laths (Figure 33). Some larger ferritic areas in this microstructure seem to be of δ-ferrite origin. TEM observations reveal the post-martensitic lath-like substructure consisting of subgrains containing recovered dislocation configurations (Figure 34) in which carbide precipitates appear in colonies along

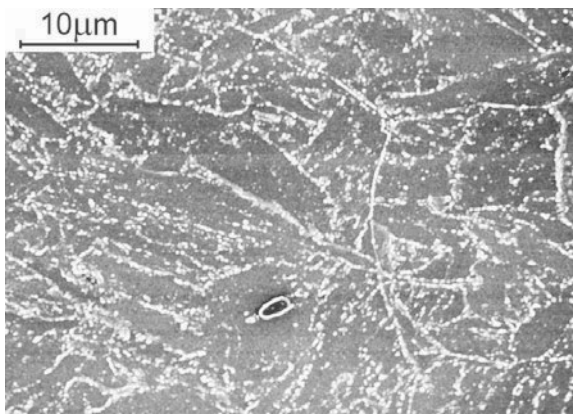

Figure 33 – High-tempered martensite in P92 steel with grain boundaries traced by precipitates; sample PM, $FeCl_3$ etched, SEM image

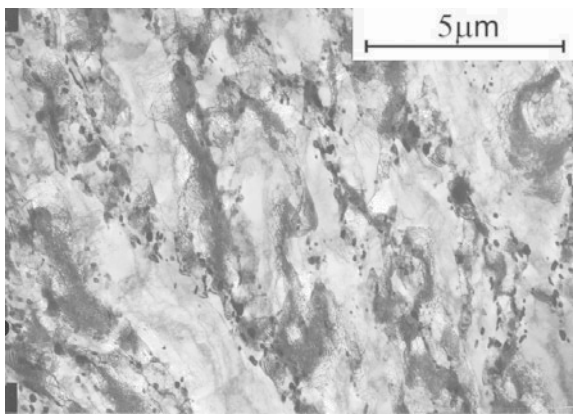

Figure 34 – Arrays of subgrains and colonies of carbides in ferritic matrix of high-tempered P92 steel; sample PM, TEM, thin foil

packages of the subgrains. High-density chains of carbides are tracing former austenite grain boundaries (Figure 35) and next to them some globular precipitate-free ferrite grains occur with networks of criss-crossing dislocations. Along the post-martensitic inter-lath boundaries mainly elongated/acicular carbides are present (Figure 36). Larger "dislocation-free" ferrite laths appear in this microstructure as well (Figure 37) and next to the borders of these laths dense colonies of coagulated carbides are present, pinning boundaries of fine subgrains (Figure 38).

After ACT at 600 °C this microstructure changes to fully recrystallized ferrite with spheroidal carbides tracing most of the former grain boundaries (Figure 39) as well as appearing inside the grains of the recrystallized ferrite (Figure 40). Continuous chains of spheroidal precipitates trace most of the former austenite grain boundaries (Figure 41). Dislocation density becomes visibly low and only small, recovered dislocation arrays or low-angle boundaries exist next to the colonies of spheroidal carbides (Figure 42), which seem to pin the boundaries.

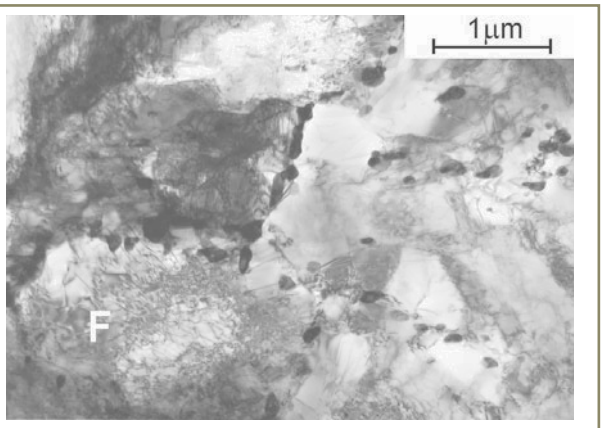

Figure 35 – Prior austenite grain boundary traced by chain of precipitates next to globular ferrite grain (F) with dislocation network; sample PM, TEM, thin foil

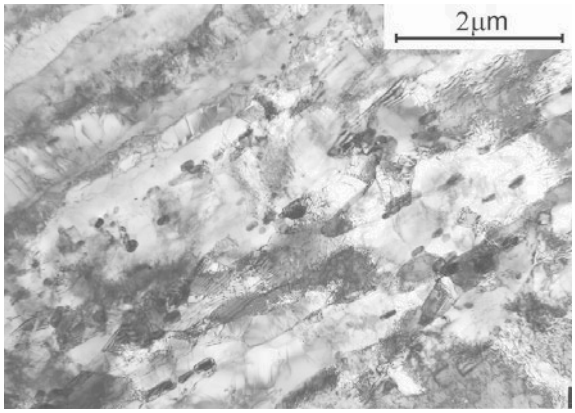

Figure 36 – Post-martensitic laths consisting of recovered subgrains with acicular carbides at inter-lath boundaries; sample PM, TEM, thin foil

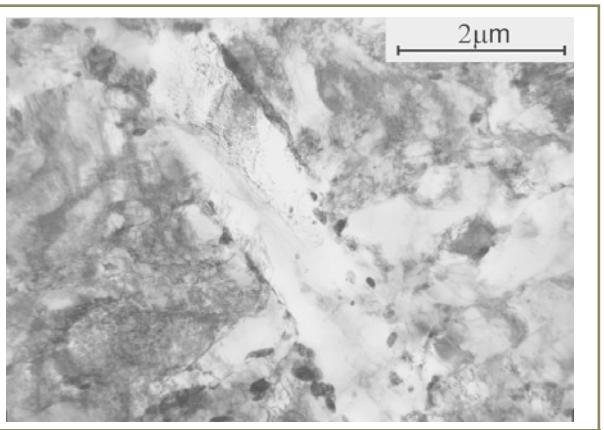

Figure 37 – Large ferrite lath with low dislocation density and colonies of carbides along its boundaries; sample PM, TEM, thin foil

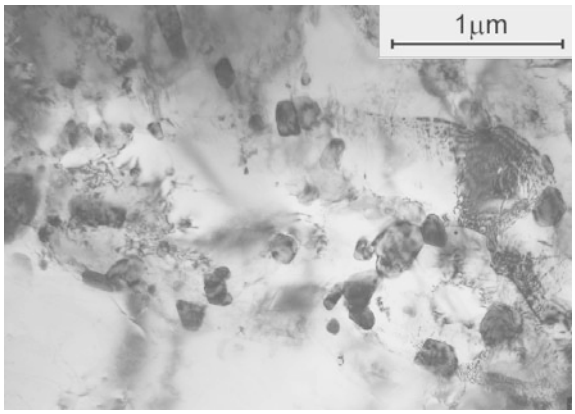

Figure 38 – A colony of coagulated carbides interacting with boundaries of small ferritic subgrains; sample PM, TEM, thin foil

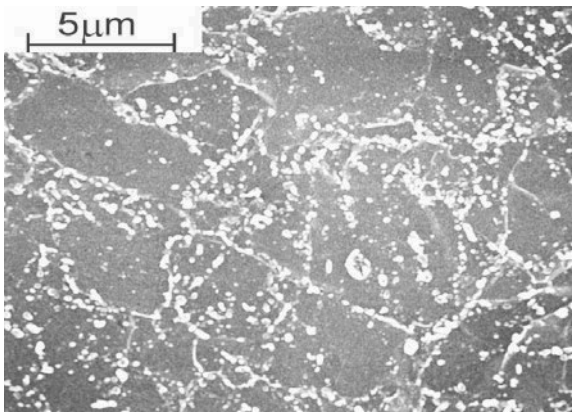

Figure 39 – Microstructure of P92 steel after ACT; precipitates along former grain boundaries; sample PM, $FeCl_3$ etched, SEM image

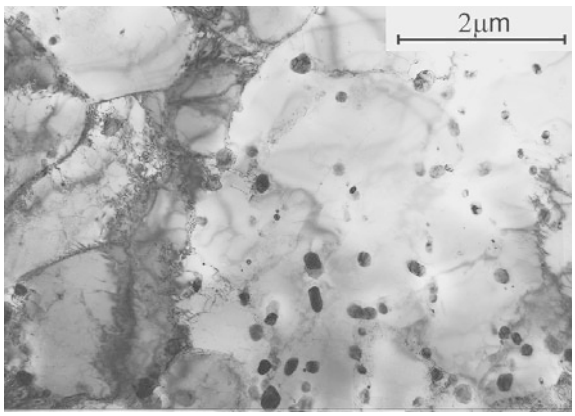

Figure 40 – Microstructure of P92 steel after ACT; spheroidal precipitates in fully recrystallized ferrite grain; sample PM, TEM, thin foil

3.5.2 Microstructure of P92 weld metal W0

In the as-received state it is a mixture of tempered martensite/bainite consisting of packages of thin post-martensitic laths near to larger post-bainitic elongated grains, all these components have high dislocation density (Figure 43). At boundaries between them appear chains of coagulated carbides and ext to such regions elongated ferrite grains exist with high dislocation density and almost no precipitates inside (Figure 44). Post-martensitic laths consist of numerous subgrains retaining their previous orientation. Small semi-recovered globular ferrite grains in former inter-bead heat-affected zones co-exist with colonies of coagulated carbides (Figure 45). In most of post-martensitic/post-bainitic subgrains and in ferrite grains appear recovered configurations of dislocations, frequently in criss-crossing pattern (Figure 46).

After ACT at 600 °C in the microstructure of weld metal sample W0, at a distance of about 2 mm from the

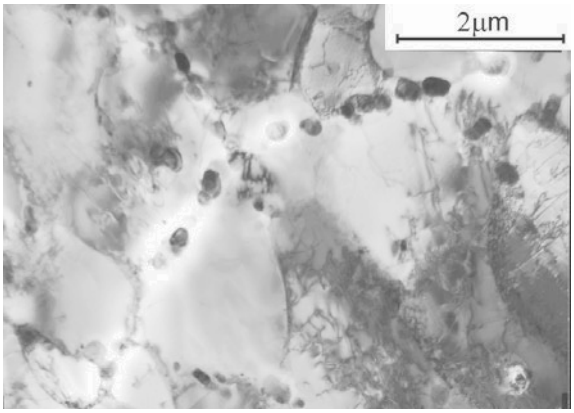

Figure 41 – Chains of spheroidal carbides along prior austenite grain boundary; sample PM, TEM, thin foil

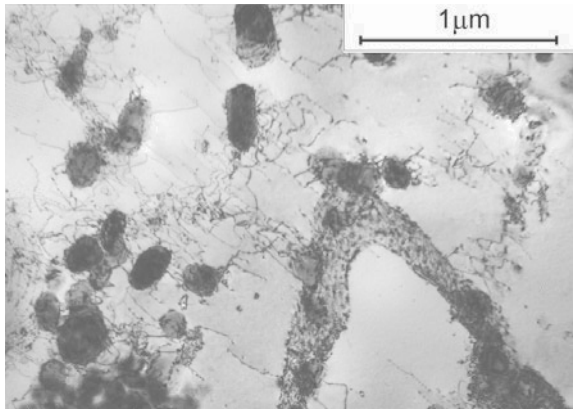

Figure 42 – Spheroidal carbides near low angle boundary and recovered dislocations near to the carbides; sample PM, TEM, thin foil

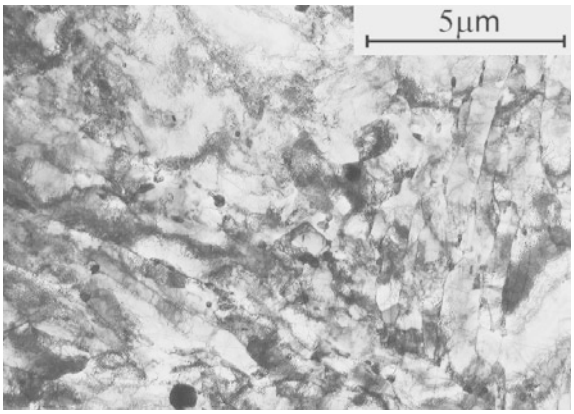

Figure 43 – Post-martensitic microstructure of weld metal W0 consisting of numerous partly recovered subgrains; TEM, thin foil

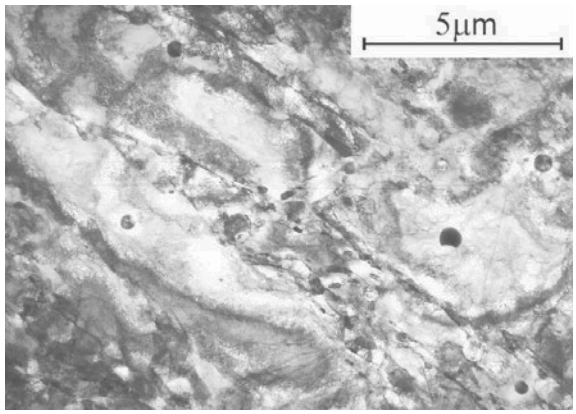

Figure 44 – Larger post-bainitic/ferritic regions of high dislocation density and chains of carbides between them; sample W0, TEM, thin foil

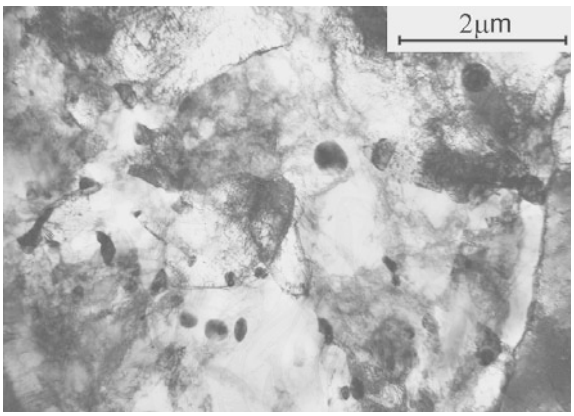

Figure 45 – Globular partly recovered ferrite grains of high dislocation density and coagulated carbides inside; sample W0, TEM, thin foil

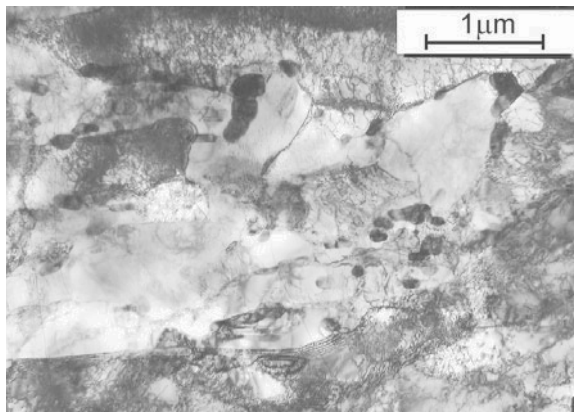

Figure 46 – Partly recovered post-martensitic subgrains containing arrays of criss-crossing dislocations; sample W0, TEM, thin foil

fracture surface, creep voids appear at carbide clusters and at inclusions (Figure 47). On etched fracture surface observed in SEM, boundaries of well recrystallized equiaxial ferrite grains and large amount of coagulated carbides can be seen (Figure 48).

As observed in TEM, the substructure after the ACT consists of recovered subgrains and small, recrystallized ferrite grains, while some of the subgrains retain their post-martensitic orientation (Figure 49) and most of the recrystallized grains appear in a fine globular form (Figure 50). Further recrystallization progresses mainly by coalescence of the subgrains. Also migration of high-angle grain boundaries can be observed and this is often retarded by coagulated/spheroidal precipitates. The subgrains as well as small, recrystallized grains have low/medium dislocation density and their boundaries are often pinned by carbides (Figure 51). In larger post-bainitic and ferritic grains high-density dislocation networks appear and at the grain boundaries very large precipitates can be found (Figure 52); few of these precipitates were identified as Laves phase.

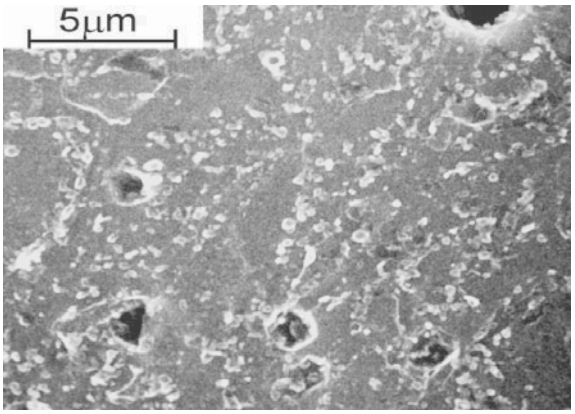

Figure 47 – Cross-section of ACT sample W0, 2 mm from fracture surface; creep voids at carbides and inclusions; $FeCl_3$ etched, SEM image

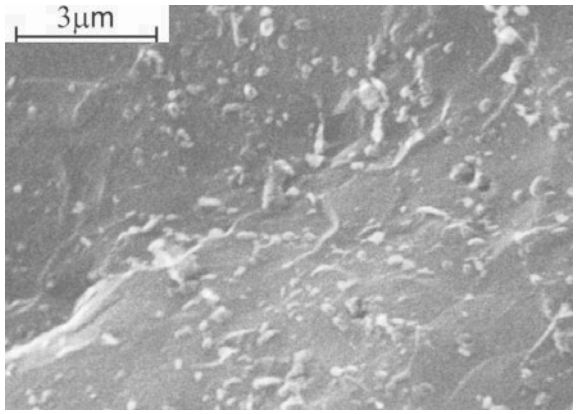

Figure 48 – ACT fracture surface of sample W0; visible coagulated precipitates and boundaries of ferrite grains: $FeCl_3$ etched, SEM image

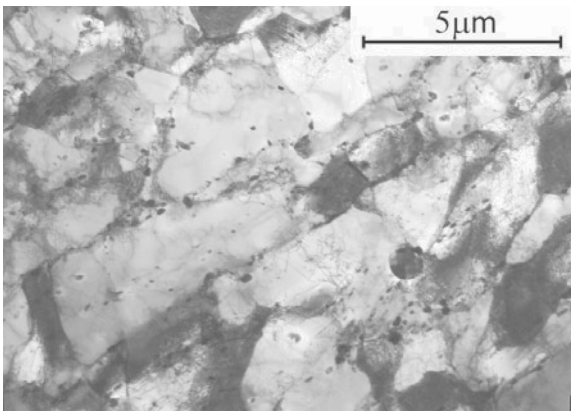

Figure 49 – Elongated subgrains and fine grains, retaining post-martensitic orientation; sample W0, TEM, thin foil

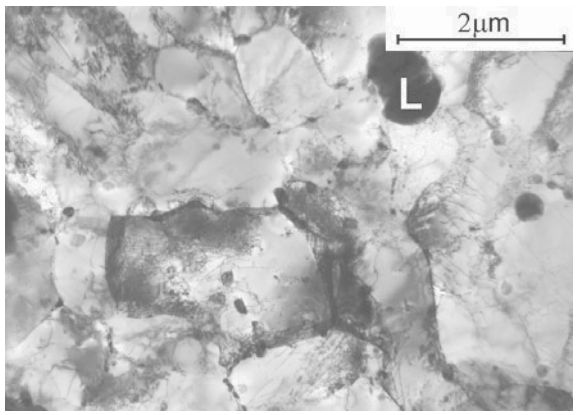

Figure 50 – Globular fine recrystallized grains and subgrains and large Laves phase precipitate (L); sample W0, TEM, thin foil

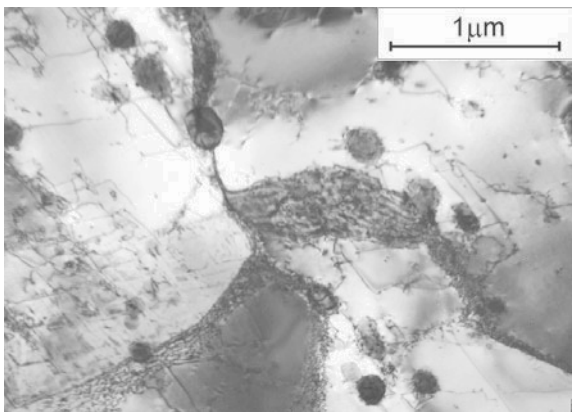

Figure 51 – Low density dislocation configurations in recrystallized ferrite subgrains; sample W0, TEM, thin foil

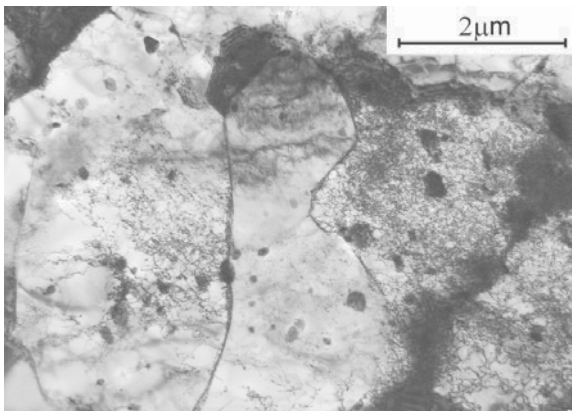

Figure 52 – High-density dislocation networks in recrystallized ferrite grains; sample W0, TEM, thin foil

4 Discussion

The main objective of this work has been to find out the reasons which caused the substantial difference of creep life of weld metal samples W1 and W2 in rupture tests at the temperature of 600 °C with load of 216 MPa; the W1 and W2 samples differed as to the content of Ti: ~300 ppm and ~700 ppm, respectively, while the amounts of other alloying elements were almost identical. The initial identification of particles carried out on carbon extraction replicas taken from these weld metals indicated substantial amounts of Ti being present in spheroidal slag inclusions but no Ti-rich carbides or carbonitrides could be found precipitated in the ferritic matrix of these samples. Observations of fracture surfaces of the creep ruptured samples revealed that the main difference between these samples was the presence in sample W1 of shear-type secondary creep cracks extending from creep voids through large ferritic, precipitate-free grains. Considering that most of these large ferritic grains were inherited from the initial δ-ferrite of the as-solidified weld metal, microhardness was tested on individual components of microstructure in the head and gauge portions of the samples W1 and W2, which revealed that after the creep rupture tests the δ-ferrite in the gauge portions, as compared with the δ-ferrite in the head portions, is softer in sample W1 while it is harder in sample W2. As the creep rupture samples should have had the uniform temperature along the whole length for the test duration, the microstructures of the grip portions of the samples could be considered as annealed only, while the microstructures of the gauge and neck portions of the creep rupture samples were certainly affected by the creep strain. This strain for both samples was substantial as their reductions of area at fracture were 78 % and 82 %, respectively for W1 and W2 [6].

In consequence of these initial findings, detailed electron-microscopic investigation was carried out with particular attention to development of dislocation substructure and associated with that precipitation processes in various components of the microstructure. For comparison with these two Ti-doped P92 weld metal, reference materials were selected available from another research [8]; these were the P92 rolled pipe PM and Ti-free weld metal W0. The microstructures of these reference samples were examined in as-delivered state and after the accelerated creep test on Gleeble. The weld metal sample W0 of 208 MPa yield strength at 600 °C, exhibited a creep life equivalent to 116 000 h/100 MPa/600 °C, as calculated from the Gleeble ACT data.

The microstructure of P92 sample PM, despite the high Cr-equivalent of 10.2, did not contain large grains of δ-ferrite. Evidently due to hot working and subsequent heat treatment applied in its manufacturing procedure, it was homogenized causing any larger primary δ-ferrite grains to disappear. Nevertheless, some finer globular ferrite grains containing characteristic dislocation networks appeared in the microstructure (Figure 35) next to high-tempered martensite features and also some laths of "grain-boundary" ferrite could be seen (Figure 37). This initial microstructure transformed quite uniformly in the accelerated creep test, resulting in fully recrystallized ferrite with spheroidal carbides all over the sample's volume. In the ferritic matrix after the ACT dominated precipitates of $M_{23}C_6$ carbides and MX carbonitrides, while large particles of Laves phase were seldom, and such final microstructure can be considered as entirely transformed.

As to the weld metal sample W0 containing no Ti additive and having low Cr-equivalent 5.8, although no δ-ferrite was seen in it, it contained numerous grain-boundary ferrite/tempered bainite features and in this sense its microstructure was initially quite inhomogeneous. Post-martensitic regions in this initial microstructure of the W0 sample consisted of well-recovered subgrains with characteristic arrays of criss-crossing dislocations and carbide precipitates along boundaries of the subgrains (Figure 46). Transformation of this microstructure during the creep test did not correct its initial inhomogeneity; next to the recrystallized fine grains of low dislocation density appeared numerous larger ferritic grains containing high-density dislocation networks of accommodation type. Evidently the shrinkage due to annihilation of defects in stronger fine-grained components of the microstructure resulted in generation of accommodation dislocations in the weaker component i.e. the larger grains of ferrite such as in Figure 52, possibly causing strain hardening of the last. In this sense the microstructure homogenized strength-wise, however it already lost its creep resistance due to complete overall recrystallization the evidence of which can be seen on the ACT fracture surface as the well-pronounced ferrite grain boundaries. These last are also evidence that the ACT was run correctly and that the sample was not broken due to an uncontrolled mechanical fatigue.

As regards the Ti-doped weld metal sample W1, its initial examined microstructure was already after 100 h of annealing at 600 °C, as was the microstructure of the head portion of the creep-ruptured sample. In its substructure dominated high-density semi-recovered dislocation arrays in every larger ferritic feature, i.e. the δ-ferrite, the grain-boundary ferrite and in the post-bainitic subgrains. Quite seldom these dislocations were pinned by fine precipitates. Such configurations of accommodation dislocations were certainly generated due to local volume changes of various microstructure components during the previous post-weld heat treatment followed by the 100 h of annealing at 600 °C. Under the influence of the creep strain in the gauge portion of the creep-ruptured sample these dislocation configurations entirely disappear creating numerous weak ferrite components. Only very few of ferrite subgrains have boundaries pinned by fine precipitates (Figure 21), while most of the large recrystallized ferrite grains appear precipitate-free. In centres of such dislocation-free recrystallized grains slag inclusions are present (Figure 20) making these sites prone to creep voids nucleation. Such nucleation was observed on fractures and cross-sections as very frequent in sample W1 (Figure 3), but not so much in sample W2 (Figure 6).

The "weak points" of sample's W1 microstructure are generally absent in sample W2. In the last the initial microstructure, i.e. after PWHT and 9 000 h of "annealing" at 600 °C, is also seriously inhomogeneous however in its grains and subgrains non-recovered high-density configurations of tangled dislocations dominate. These configurations under influence of the creep strain, i.e. in the gauge portion of the sample, do recover, however they simultaneously become pinned by ultra-fine precipitates in numerous locations, in particular in the δ-ferrite in which this strain-induced precipitation causes its hardening (Figure 30 and see Table 4). Also the boundaries of recovering subgrains become intensively pinned by the ultra-fine precipitates (Figure 28). Confirmation of the strain-induced precipitation can be gained from comparing substructures in thin foils taken from the neck part of the gauge portion at a distance of about 1.5 mm from the fracture and from the uniformly extended part of the gauge portion at the location of ~6 mm from the fracture. The substructures at the first place, representative of a 63 % reduction of area on the creep-ruptured sample W2, have much more intensive precipitation of ultra-fine particles on dislocations (Figures 31 and 32) than the substructures of similar ferrite grains being in the gauge portion further away from the fracture, i.e. at the location where reduction of area is about 40 % (Figures 29 and 30).

The observed high intensity strain-induced precipitation seems to be the most important factor contributing to the long life of sample W2 in the creep rupture test and the associated high potential of precipitation hardening equalizing the strength of all components of the weld metal matrix indicates peculiar "hidden homogeneity" of this matrix evidently affected by the welding procedure and the subsequent PWHT. This cannot be said about sample W1 of which the initial microstructure, additionally affected by the 100 h of annealing at 600 °C in its head portion during the creep rupture test, does not have such precipitation potential and moreover contains microstructural features prone to faster creep cavitation and cracking. This in particular refers to the large grains of δ-ferrite which, although strain-hardening a bit after the creep test, do not seem to adequately precipitation strengthened, and also to the characteristic elongated ferritic features appearing in the microstructure along the re-austenitized grains (Figures 7 and 11). These narrow ferrite laths are susceptible to shear-type creep cracking extending along them (Figure 3).

Not too much can be concluded from the microanalytical research; certain increase of alloying elements content in $M_{23}C_6$ carbides on the expense of Fe in sample W2 as compared with W1 is evident and results from much longer annealing time at 600 °C – 9 000 h vs. 100 h. The available microanalytical facility did not allow measuring quantitatively the contents of alloying elements in the components of the matrix of the considered weld metals, while the chemical composition of the matrix and stored energy in it are responsible for intensity of precipitation hardening during the long-term exposure to creep. Finally, the role of the imposed stress (of 216 MPa) in the creep rupture test cannot be ignored. This stress being at the level of yield stress at the creep rupture test temperature of 600 °C certainly contributed to substantial reduction of area of the crept samples and evidently accelerated the strain-induced precipitation, so the non-answered question remains whether this "forced" precipitation contributed to the exceptional long life of sample W2 in the creep test and, if yes, then how much.

Regarding sample W1, its "premature" failing after only 100 h in the creep rupture test, despite the large content of weak ferritic features, seems also associated with the dislocation substructures in these weak components, which consist of highly-mobile dislocations easy to recover and annihilate very fast. Intentional generation of such dislocation substructures stands behind the concept of the accelerated creep test on Gleeble (see Figure 52 and [10]). Here in the case of weld metal W1 which already in the initial state contains such dislocation configurations in large amount, the origins of them can be described as the combination of welding procedure enhancing the local segregations of alloying elements, and then, excessive PWHT which next to tempering of stronger microstructural components caused in the weaker components generation of highly-mobile accommodation dislocations contributing to fast loss of creep resistance.

5 Conclusions

W1 weld metal, with "base-line" Ti content in its initial state, comprised large amounts of weak pure ferritic components of microstructure, not strengthened by precipitates and containing configurations of unpinned highly-mobile dislocations, and during the creep rupture test the creep voids and creep cracks formed fast and preferentially in these weak components.

W2 weld metal, with "medium" Ti content, was in its initial state microstructurally more homogeneous than W1 and the dislocation substructure in most of its potentially weak ferritic components mainly consisted of tangled non-recovered configurations; this initial substructure and imposed strains participated in strain-induced precipitation during the creep rupture test.

For such Ti-containing weld metals further study on optimization of welding procedures is needed, in order to reduce the initial segregation of alloying elements and to control the formation of the weak components of microstructure. This refers also to PWHT, which must not additionally reduce the creep strength of the already weak components of microstructure.

Acknowledgements

Thanks of the authors are extended to Dr D.J. Abson of TWI, Abington/Cambridge, UK, for providing samples W1 and W2 as well as important information to this investigation. Also the support of this research from the Slovak Academy of Sciences is here gratefully acknowledged.

References

[1] Mandziej S.T. and Výrostková A.: Evolution of Cr-Mo-V weld metal microstructure during creep testing - Part 1: P91 material, Doc. IIW-1822, Welding in The World, 2008, vol. 52, no. 1/2, pp. 3-26.

[2] Brett S.J., Allen D.J. and Buchanan L.W.: The Type IV creep strength of grade 91 materials, Conference Proceedings, Integrity of High Temperature Welds, IOM3, London, April 2007, pp. 409-419.

[3] Kimura K., Sawada K., Kushima H. and Toda Y.: Influence of composition partitioning on creep strength of high chromium ferritic creep resistant steels, Conference Proceedings, Integrity of High Temperature Welds, IOM3, London, April 2007, pp. 421-430.

[4] Zhang Z., Marshall A.W. and Holloway G.B.: Flux-cored arc welding: The high productivity welding process for P91 steels; Proceedings of the 3rd EPRI Conference on Advances in Materials Technology for Fossil Power Plants, Swansea, April 2001.

[5] Chovet C., Galand E. and Leduey B.: Effect of various factors on toughness in P92 SAW weld metal, IIW Doc. II-C-341-07, 2007.

[6] Abson D.J., Rothwell J.S. and Woollin P.: The influence of Ti, Al and Nb on the toughness and creep rupture strength of grade P92 steel weld metal, Conference Proceedings, Integrity of High Temperature Welds, IOM3, London, April 2007, pp. 129-138.

[7] Abson D.J., TWI, Abington – Cambridge, UK, private communication, 2005.

[8] Mandziej S.T.: Advanced materials analysis, Enschede, NL, unpublished contracted research, 2008.

[9] Patriarca P., Harkness S.D., Duke J.M. and Cooper L.R.: US advanced materials development program for steam generators, Nuclear Technology, 1976, vol. 28, no. 3, pp. 516-536.

[10] Mandziej S.T.: Accelerated creep test on Gleeble – State of the art, IIW Doc. II-1717-09, 2009.

About the authors

Dr. Stan T. MANDZIEJ (stanamanl@cs.com) is with Advanced Materials Analysis, Enschede (The Netherlands). Dr. Anna VYROSTKOVA (avyrostkova@imr.saske.sk) is with the Institute of Materials Research SAS, Kosice, (Slovakia). Dr. Corinne CHOVET (corinne.chovet@airliquide.com) is with Air Liquide – CTAS, Saint-Ouen l'Aumône (France).